Accounting for Localized Defects in the Optoelectronic Design of Thin-Film Solar Cells

Michael G. Deceglie, Vivian E. Ferry, A. Paul Alivisatos, and Harry A. Atwater

***Abstract*—Controlled nanostructuring of thin-film solar cells offers a promising route toward increased efficiency through improved light trapping. Many such light trapping designs involve structuring of the active region itself. Optimization of these designs is aided by the use of computer simulations that account for both the optics and electronics of the device. We describe such a simulation-based approach that accounts for experimental tradeoffs between high-aspect ratio structuring and electronic material quality. Our model explicitly accounts for localized regions of degraded material quality that is induced by light trapping structures in n-i-p a-Si:H solar cells. We find that the geometry of the defects couples to the geometry of light absorption profiles in the active region and that this coupling impacts the spectral response of the device. Our approach yields insights into the nanoscale device physics that is associated with localized geometry-induced defects and provides a framework for full optoelectronic optimization.**

***Index Terms*—Light trapping, plasmon, simulation, thin-film solar cell.**

I. Introduction

An important challenge in the development of thin-film solar cells is the optimization of light trapping design. Thin absorber layers can be less expensive to fabricate and can offer electrical advantages over thick devices [1]–[4]. In order to achieve the high efficiencies that are required to make such technologies competitive with traditional wafer-based solar cells, it is critical to optimize both their optical and electrical performance. While thin-film silicon solar cells typically rely on randomly textured substrates to achieve light trapping [5], [6], significant attention has recently been directed toward designed nanostructuring of solar cells, which offers increased control of light absorption and propagation in the device [2], [3], [7]–[24]. Design of such structures is aided by the use of computer simulations that account for both optical and electrical performance of the device [8], [25].

Many promising nanophotonic designs involve structuring of the active layers themselves [3], [14]–[24]. Such approaches can offer enhanced light trapping through antireflection effects, resonant absorption in semiconductor nanostructures, and improved control over the optical mode structure in the active layer [3], [15]. It is important to note thatthe deposition of highly structured active layers can produce localized regions of low material quality, resulting in a tradeoff between enhanced optical design and optimized material quality [20], [22], [26]–[28]. Thus, in order to optimize device efficiency, it is, important to consider the effect of morphologically induced local defects when designing and optimizing light-trapping nanostructures [22].

The focus of this study is to demonstrate that such local defects can be accounted for in multidimensional optoelectronic simulations of nanostructured thin-film a-Si:H solar cells. Explicitly accounting for local variations in material quality in these simulations provides physical insight into the microscopic device physics governing operation. In particular, we find that defect location can couple to the optical excitation profile in the device, which results in a spectral response different from that obtained when uniform material quality is assumed.

Our approach is based on coupled optical and electrical simulations in which the optical generation rate is calculated from full-wave electromagnetic simulations and taken as input into a finite-element method (FEM) device physics simulation [8], [29]. This method has been shown to reproduce experimental current–density voltage curves of a-Si:H solar cells that feature light trapping nanospheres [30]. In the electrical simulation step, we address the tradeoff between optical design and electrical material quality by including a localized region within the a-Si:H exhibiting increased dangling bond trap density. This region of degraded material represents a recombination active internal surface (RAIS) that is formed during deposition. Such localized regions of low-density low-electronic-quality material quality are known to form during plasma enhanced chemical vapor deposition (PECVD) when growing surfaces collide with one another during deposition, a process that is particularly likely in the high-aspect ratio features used for light trapping [20], [22], [26], [27].

II. Simulation Details

The structure we investigated is shown in Fig. 1. The design is based on an n-i-p a-Si:H device in which all layers are conformally deposited over a nanostructured substrate. Our approach

Manuscript received May 22, 2012; accepted January 8, 2013. Date of publication February 5, 2013; date of current version March 18, 2013. This work was supported by the "Light–Material Interactions in Energy Conversion" Energy Frontiers Research Center, United States Department of Energy, under grant DE-SC0001293, LBL Contract DE-AC02–05CH11231. The work of M. G. Deceglie was supported by the Office of Basic Energy Sciences under Contract DOE DE-FG02–07ER46405 and the National Central University's Energy Research Collaboration.

M. G. Deceglie and H. A. Atwater are with the Thomas J. Watson Laboratories of Applied Physics, California Institute of Technology, Pasadena, CA 91125 USA (e-mail: deceglie@caltech.edu; haa@caltech.edu).

V. E. Ferry and A. P. Alivisatos are with the Materials Science Division at Lawrence Berkeley National Laboratory and the Department of Chemistry, University of California, Berkeley, CA 94720 USA (e-mail: veferry@lbl.gov; apalivisatos@lbl.gov).

Color versions of one or more of the figures in this paper are available online at http://ieeexplore.ieee.org.

Digital Object Identifier 10.1109/JPHOTOV.2013.2240764

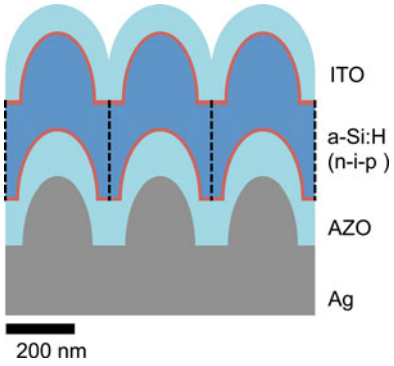

Fig. 1. Schematic showing the geometry of simulated n–i–p a-Si:H solar cell. The red regions indicate the doped a-Si:H. The dashed lines indicate the location of RAISs, which are accounted for in the model as local regions of degraded material quality extending vertically through the device.

is to first carry out single-wavelength full-wave optical simulations with the finite-difference time-domain (FDTD) method. The carrier generation profile in the a-Si:H is extracted from the FDTD results for each wavelength and is weighted by the AM1.5G spectrum. The resulting white-light generation profile is then taken as input into an FEM device physics simulation in which the electrostatic and carrier transport equations are numerically solved in the a-Si:H region to extract the current density–voltage (J–V) characteristics of the device. From the simulated J–V curve, we extract the open circuit voltage $V_{\rm oc}$, the short circuit current density $J_{\rm sc}$, the fill factor FF, and the resulting conversion efficiency. We also use the single-wavelength generation profiles as input into short-circuit calculations to simulate spectral external quantum efficiency (EQE) of the device. This approach accounts for the full microscopic device physics of carrier collection under illumination and bias in complex geometries.

The structures are based on, from bottom to top, 200 nm of nanostructured Ag, a 130-nm-thick aluminum-doped zinc oxide (AZO) layer, an n-i- p a-Si:H active region with 10-nm-thick n and p layers and 270 nm i-layer, and an 80 nm indium-doped tin oxide (ITO) layer. All the upper layers are assumed to conformally coat the textured Ag. The Ag features are 200 nm wide, the AZO and a-Si:H features are 220 nm wide, and the ITO features are 300 nm wide. The pitch of the features is 300 nm, the closest packing achievable without overlap of the ITO features. The height of the raised features is 200 nm in all layers. The simulations in this study are done in 2-D to take advantage of reduced computational demand, but we note that the methods are applicable to full 3-D simulations as well [8]. We note that the schematic in Fig. 1 is three simulation volumes wide. The explicit simulation volume is that between neighboring dashed lines, and Neumann boundary conditions are imposed at the horizontal boundaries to model the periodic structure. In all plots of spatial results that are presented here, we have stitched together three copies of the simulated region in order to help the reader visualize the periodic structure that is implied by the boundary conditions.

The first step in our approach is to carry out optical simulations by numerically solving Maxwell's equations with a commercial FDTD simulation package [31]. Single-wavelength simulations are carried out at 10 nm increments in wavelength between 350 and 800 nm. Both transverse electric and transverse magnetic polarizations of incident light are simulated, and the results are averaged to model unpolarized sunlight. The optical constants for ITO, AZO, and a-Si:H were taken from experimental measurements [3]. The optical constants for Ag were obtained from a Lorentz–Drude fit to values given by Palik [32] as described by Rakic *et al.* [33]. Each single-wavelength (at wavelength λ) simulation results in an optical field intensity, $|E(\vec{r},\lambda)|^2$, profile in the simulated structure. We then calculated the wavelength-dependent generation rate, profile, $G_{\rm opt}(\vec{r},\lambda)$, in the a-Si:H using

$$G_{\rm opt}(\vec{r},\lambda) = \frac{\varepsilon'' \left|E(\vec{r},\lambda)\right|^2}{2\hbar} \tag{1}$$

derived from the divergence of the Poynting vector, where ε'' is the imaginary part of the permittivity. These single-wavelength generation profiles were weighted by the AM1.5G spectrum to obtain a one-sun white-light generation profile $G_{\rm opt}(\vec{r})$, within the a-Si:H.

To connect the optical simulations to the device physics simulation, we then interpolated the carrier generation profiles in the a-Si:H region onto a finite-element mesh for the calculation of the *J–V* characteristics under illumination. Then, the electrical simulations were carried out with a commercial technology computer-aided design (TCAD) software package [34] that numerically solves the electron (2) and hole (3) continuity equations

$$\frac{\partial n(\vec{r})}{\partial t} = G(\vec{r}) - U(\vec{r}) + \frac{1}{q}\nabla \cdot \vec{J}_n(\vec{r}) \tag{2}$$

$$\frac{\partial p(\vec{r})}{\partial t} = G(\vec{r}) - U(\vec{r}) - \frac{1}{q}\nabla \cdot \vec{J}_p(\vec{r}) \tag{3}$$

the transport equations for electrons (4) and holes (5)

$$\vec{J}_n(\vec{r}) = q\mu_n n(\vec{r})\vec{E}(\vec{r}) + qD_n \nabla n(\vec{r}) \tag{4}$$

$$\vec{J}_p(\vec{r}) = q\mu_p p(\vec{r})\vec{E}(\vec{r}) - qD_p \nabla p(\vec{r}) \tag{5}$$

and Poisson's equation

$$\nabla \cdot \vec{D}(\vec{r}) = \rho_f(\vec{r}) \tag{6}$$

for the electrostatics. In (2)–(6), n and p are the electron and hole concentrations, G is the generation rate, q is the elementary charge, $\vec{J}_n$ and $\vec{J}_p$ are the electron and hole current densities, respectively, μ_n and μ_p are the electron and hole mobilities, respectively, $\vec{E}$ is the electrostatic field, D_n and D_p are the electron and hole diffusion coefficients, respectively, and $\vec{D}$ is the electric displacement. The generation profiles that are calculated via FDTD are taken as input into the continuity equations. The recombination rate U is calculated with a model that is included in the TCAD software package that explicitly calculates the statistics of trap occupation, trap-mediated recombination, and charge state along with the associated electrostatics [34].

We only simulated the a-Si:H regions electrically, and the boundary conditions at the contacts are assumed to be ohmic contacts to the n- and p-type regions. We also include a 5 Ω cm^2

series resistance at the top contact and a shunt resistance (parallel to the device) of 5 kΩ cm^2 with the built-in TCAD circuit simulation capabilities. The bandgap was taken to be 1.78 eV in all regions with a 4 eV electron affinity. The active dopant concentration in the doped regions was 3×10^{19} cm^{-3}·eV^{-1}. All other electronic material parameters are taken to be the values that are suggested by Schropp and Zeman [35]. We included distributions of traps throughout the bandgap to represent band tail (exponential distribution from each band edge) and dangling bond (Gaussian mid-gap distribution) states. The parameters for the trap distributions are based on those described by Schropp and Zeman [35], with the exception that the peak dangling bond density in the intrinsic a-Si:H was taken to be 2×10^{17} cm^{-3}·eV^{-1} to account for the experimental observation that $V_{\rm oc}$ decreases with the increase in intrinsic layer thickness [3]. The full trap parameters as implemented in our simulations have been previously described [8]. Simulation of a perfectly flat device with the layer thicknesses that are described above and these material parameters yields a conversion efficiency of 5.81%, $J_{\rm sc}$ of 8.82 mA cm^{-2}, $V_{\rm oc}$ of 943 mV, and FF of 70.4.

To explicitly account for the effects of RAISs, we include 5-nm-wide vertical strips of defective a-Si:H that extends through all the active regions of the device. In these RAIS strips, we specified an increased peak dangling bond density of 2×10^{20} cm^{-3}·eV^{-1}. The dashed lines in Fig. 1 show the location of the RAISs. The explicit width of each simulated RAIS is 2.5 nm; since it is located on the edge of the simulation volume, the Neumann boundary conditions give it an implied width of 5 nm by symmetry. Our assumption that these low-density regions are characterized by an increased dangling bond density is justified by experiments showing that a-Si:H solar cells with increased concentrations of microvoids showed degraded performance that was attributed to an increase in dangling bond density [36]. We found that the peak dangling bond density that is specified in the RAISs results in device performance similar to that obtained by specifying a surface recombination velocity (SRV) of 10^6 cm·s^{-1} at the interface between the RAISs and the bulk a-Si:H. Specifying an SRV of 10^6 cm·s^{-1} yields a 5.86% efficient device compared with an efficiency of 5.90% with a peak trap density of 2×10^{20} cm^{-3}·eV^{-1} in the RAISs region (the value used throughout this study). We prefer the explicit inclusion of traps in the model because it more closely represents the fundamental physical mechanism that underlie the recombination activity of the RAISs.

For white-light *J–V* simulation, we take the AM1.5G weighted generation profile $G_{\rm opt}(\vec{r})$, as input into the continuity (2) and (3). The *J–V* curve is then swept by quasistatically varying the voltage boundary conditions at the contacts. We also simulate the spectral response of the device by the calculation of the short circuit current due to the single-wavelength generation profiles, $G_{\rm opt}(\vec{r},\lambda)$. For the spectral response simulations, illumination power at each wavelength is 10 mW·cm^{-2}. This power was previously found not to alter the device physics of short circuit charge carrier collection when compared with AM1.5G illumination [8].

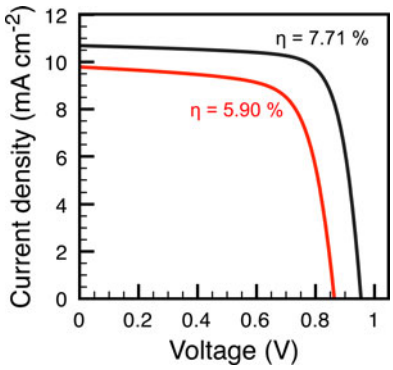

Fig. 2 Current density–voltage curves showing the simulated change in performance between the case in which no material degradation is assumed (black) and the case in which RAISs are included. The conversion efficiencies are noted on the plot.

III. Results and Discussion

We begin by comparing the *J–V* characteristics of identical devices with and without RAISs. These *J–V* curves are shown in Fig. 2. In agreement with experimental reports [22], [26], [27], the introduction of RAISs is found to adversely affect performance. When RAISs are included in the electrical simulation, the AM1.5G energy conversion efficiency is reduced from 7.71% to 5.90%, $J_{\rm sc}$ from 10.69 to 9.79 mA·cm^{-2}, $V_{\rm oc}$ from 0.954 to 0.864 V, and FF from 76.3 to 70.4. To determine if the reduced $V_{\rm oc}$ is due to the reduced $J_{\rm sc}$, we also simulated the cell without RAISs and with the generation profile $G_{\rm opt}(\vec{r})$, uniformly scaled down by a factor of 0.9158. This resulted in $J_{\rm sc}$ matched to that of the case that includes RAISs (9.79 mA cm^{-2}). In this case, however, $V_{\rm oc}$ was only reduced by 3 mV, to 0.951 V, and the FF remained 76.3. This indicates that the reduction in $V_{\rm oc}$ cannot be directly attributed to the reduced $J_{\rm sc}$ that is associated with the RAIS.

Studying the simulated spectral response of these devices reveals interactions between the generation profile and the geometry of the device and RAISs themselves. Fig 3(a) shows the simulated EQE as a function of wavelength for three cases: 1) a control in which the a-Si:H is assumed to maintain high quality, with a peak dangling bond density in the intrinsic region of 2×10^{17} cm^{-3}·eV^{-1}; 2) the RAIS case described in Section II; and 3) a device in which the intrinsic a-Si:H has a uniformly degraded material quality without explicitly considering localized defects. In the third case, the peak dangling bond density in the intrinsic region is increased to 1.08×10^{18} cm^{-3}·eV^{-1}, which was chosen because it results in a white-light device efficiency of 5.90%, identical to that obtained in the RAIS case. (The uniformly degraded cell exhibits $J_{\rm sc}$ of 10.18 mA·cm^{-2}, $V_{\rm oc}$ of 0.880 V, and FF of 66.4 under AM1.5G illumination.) This allows us to compare a case where optical design interacts with a localized defect to a case where the degradation is global throughout the film. Fig. 3(a) shows that both the uniform and RAIS cases exhibit degraded spectral response when compared with the control case. However, we also note that the RAIS and uniform degradation EQE curves vary from one another.

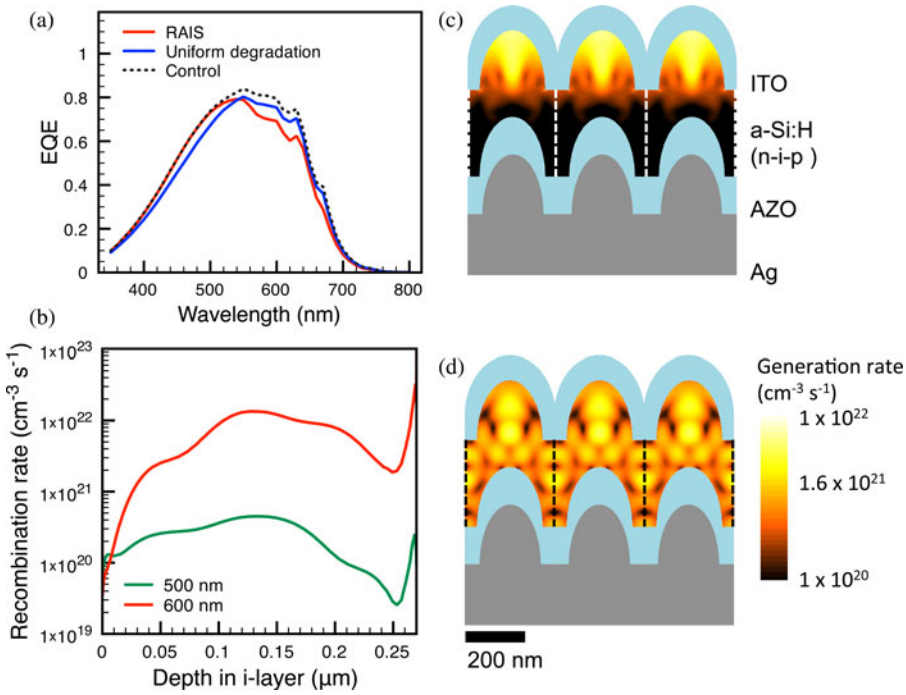

Fig. 3 Spectral coupling between optics and defect geometry. (a) Simulated EQE for a device with no assumed material degradation (control), a device with the i-a-Si:H uniformly degraded, and a device with RAISs. We note that the EQE curves for the uniform degradation and RAIS case differ from one another. (b) Recombination rate in the RAIS region plotted as a function of depth in the i-layer (with 0 being the p/i interface) for single-wavelength illumination at 500 and 600 nm. (c) and (d) Generation rate profile for single-wavelength illumination at 500 and 600 nm, respectively. We note that under 500 nm illumination, the EQE for the control and RAIS cases exhibit very small deviations from one another, while at 600 nm, the RAIS EQE is significantly degraded. We attribute this to increased optical generation in the vicinity of the RAISs at 600 nm illumination, leading to more recombination in the RAIS and thus decreased EQE.

To understand this effect, we compare the internal device physics for the RAIS case under two illumination wavelengths: 500 nm, at which there is negligible deviation between the RAIS case and the control, and 600 nm, at which the RAIS case exhibits degraded EQE. In both the uniform degradation and RAIS cases, the optical generation profile at each wavelength is identical; therefore, differences are due to electrical properties. By comparing the recombination activity within the RAIS region at these illumination wavelengths, as shown in Fig. 3(b), we see that the recombination activity is significantly higher at 600 nm wavelength illumination. Fig. 3(c) and (d) shows that under 600 nm illumination, much more optical generation is taking place in and around the RAIS than at 500 nm illumination. Thus, we attribute both the spectral variation in RAIS recombination activity and the deviations between the RAIS and uniform degradation EQE curves to interaction between the geometry of the generation profile and geometry of the RAIS. If there is a large amount of optical generation in and around the RAIS, this leads to an increase in RAIS recombination activity and a corresponding decrease in EQE.

To quantify the effect of this optoelectronic interaction under AM1.5G illumination, we compare the results of the full white-light simulation of the RAIS case to a case in which we assume a constant uniform optical generation rate of 3.04×10^{21} $\mathrm{cm}^{-3}\cdot\mathrm{s}^{-1}$; this generation level was chosen because it produces the same J_{sc} as the realistic simulation that includes the nonuniform generation profile that is associated with the light trapping nanostructures. While somewhat unphysical, this uniform generation case allows us to understand the effect of the interaction between the RAIS geometry and the optical generation profile. We define a quantity, the optical generation current density in the intrinsic region, $J_{\mathrm{opt},i}$, which is an equivalent electrical current that is calculated from the spatially integrated white-light generation profile, $G_{\mathrm{opt}}(\vec{r})$, over the intrinsic a-Si:H region assuming unity carrier collection efficiency. It is well known that carrier collection is poor from the doped regions; thus, the intrinsic layer is the region of interest. We observe that the ratio $J_{\mathrm{sc}}/J_{\mathrm{opt},i}$ changes from 0.88 for the full optoelectronic simulation to 0.80 for the uniform generation simulation. If we carry out the same procedure for the case without the RAISs, the ratio $J_{\mathrm{sc}}/J_{\mathrm{opt},i}$ remains high, changing from 0.96 to 0.95. This shows that the interaction between microstructure and optical generation profile is not limited to single-wavelength illumination, but it also affects the internal quantum efficiency of charge collection under full AM1.5G illumination. It is particularly important to account for this interaction in periodic structures, such as that studied here since both the generation profile and the defect structure are periodic.

This geometric interaction between the optics and electrical device physics can only be captured with multidimensional modeling. Furthermore, this effect illustrates the importance of accounting for defect geometry, and that approximations that involve uniformly degraded active material to account for localized defects do not fully capture the optoelectronic device physics. We note that several 1-D device simulation tools have been widely and successfully used to simulate and study solar

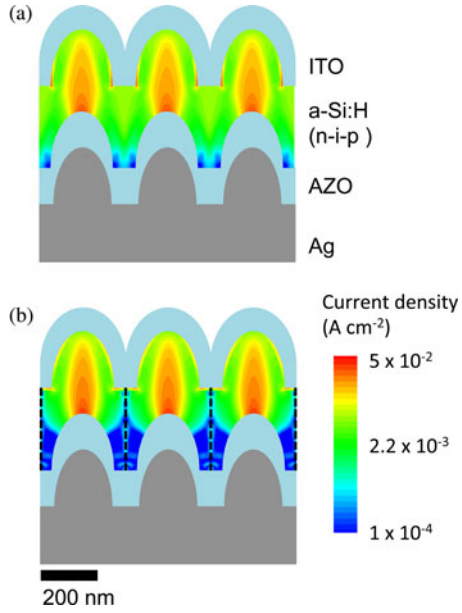

Fig. 4 Simulated magnitude of the current density within the a-Si:H at the maximum power point operating bias of the respective device under AM1.5G illumination for (a) control case with no material degradation (operating bias: 792 mV) and (b) RAIS case (operating bias: 690 mV). We note that current is suppressed near the RAIS itself, while collection from other areas of the device is not significantly impacted.

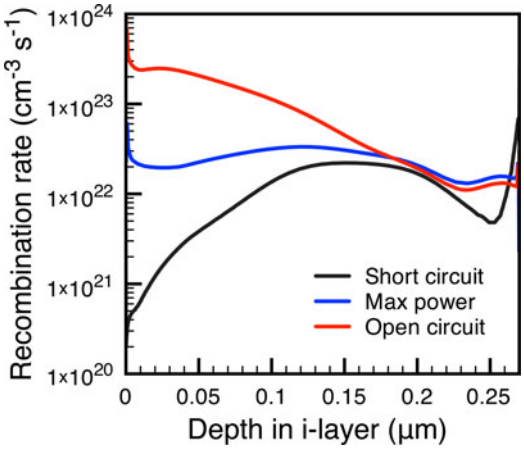

Fig. 5 Simulated recombination rate in the RAIS region plotted as a function of depth (with 0 being the p/i interface) in the intrinsic a-Si:H layer, at short circuit, maximum power operating point (690 mV), and open circuit (864 mV). The recombination activity in the defective RAIS region is shown to increase as the forward bias is increased.

cell performance in a variety of applications [37]–[41]. However, this interaction between optics and defect geometry is inherently multidimensional and cannot be captured with a 1-D simulation.

This modeling approach also provides insights into the microscopic device physics of the RAIS under 1 sun AM1.5G illumination. Fig. 4 shows the magnitude of the current density within the a-Si:H in the device without [see Fig. 4(a)], and with [see Fig. 4(b)] RAISs at the respective maximum power point operating voltage. We observe local reduction in current density in the region around the RAIS [see Fig. 4(b)] when compared with the control case [see Fig. 4(a)]. This shows that current flow in the bulbous regions (which are assumed to be high-quality a-Si:H) remains largely unperturbed by the addition of the RAISs, and that the detrimental effects of the RAIS are localized to the immediate region that surrounds them.

Fig. 5 shows the recombination activity in the RAIS as a function of operating bias under AM1.5G illumination. We see that as the device is forward biased, the recombination rate in the defective RAIS region increases. This is expected, since carrier collection form the absorber is necessarily less efficient as the device is forward biased and the built-in electrostatic field driving carrier collection is reduced, which enables more carriers to recombine in the highly defective RAIS region before being collected. It is interesting to note that most of this increase in recombination activity occurs near the front of the device. We emphasize that this is purely a result of the solution to the electrostatic, current, and continuity equations (2)–(6) under the changing contact boundary conditions, and is not due to any assumed change in the physical or electronic structure of the RAIS regions themselves under forward bias.

IV. Conclusion

We have demonstrated the use of coupled multidimensional optical and electrical simulations for the study of the optoelectronic device physics of localized defects that are induced by nanostructures in thin-film solar cells. In addition to providing a detailed picture of the microscopic device physics affecting carrier collection, our results highlight the importance of accounting for the specific geometry of the defects themselves along with the full optical absorption profile within the device. In particular, we found that interactions between the geometry of the absorption profile and the RAISs can induce significant variations in carrier collection efficiency. Such effects cannot be fully accounted for without implementing a multidimensional model such as that used here.

It is critical to account for tradeoffs between optical and electrical performances in the optimization of light-trapping structures for solar cells. This prevents the unconstrained optimization of the optical properties of a device from yielding impractical geometries that suffer severe material quality degradation. The method that we present could be coupled to an empirical study on morphologically dependent material quality for a specific process in order to fully understand and optimize the optoelectronic design of thin-film solar cells. Furthermore, our general approach of multidimensional optoelectronic simulations that include local variations in material parameters is applicable to other photovoltaic material systems in addition to a-Si:H. Our approach provides a framework within which light trapping designs for different photovoltaic material systems, which are governed by different practical limitations, can be optimized.

Acknowledgment

The authors would like to thank M. Kelzenberg and D. Turner-Evans for useful discussions regarding technical aspects of the simulations.

REFERENCES

[1] M. A. Green, "Limits on the open-circuit voltage and efficiency of silicon solar cells imposed by intrinsic auger processes," *IEEE Trans. Electron Devices*, vol. 31, no. 5, pp. 671–678, May 1984.

[2] V. E. Ferry, J. N. Munday, and H. A. Atwater, "Design considerations for plasmonic photovoltaics," *Adv. Mater.*, vol. 22, pp. 4794–808, Nov. 16, 2010.

[3] V. E. Ferry, M. A. Verschuuren, H. B. T. Li, E. Verhagen, R. J. Walters, R. E. I. Schropp, H. A. Atwater, and A. Polman, "Light trapping in ultra-thin plasmonic solar cells," *Opt. Exp.*, vol. 18, pp. A237–A245, 2010.

[4] A. V. Shah, H. Schade, M. Vanecek, J. Meier, E. Vallat-Sauvain, N. Wyrsch, U. Kroll, C. Droz, and J. Bailat, "Thin-film silicon solar cell technology," *Progress Photovoltaics: Res. Appl.*, vol. 12, pp. 113–142, 2004.

[5] J. Müller, B. Rech, J. Springer, and M. Vanecek, "TCO and light trapping in silicon thin film solar cells," *Solar Energy*, vol. 77, pp. 917–930, 2004.

[6] C. Rockstuhl, S. Fahr, K. Bittkau, T. Beckers, R. Carius, F. J. Haug, T. Sderstrm, C. Ballif, and F. Lederer, "Comparison and optimization of randomly textured surfaces in thin-film solar cells," *Opt. Express*, vol. 18, pp. A335–A341, 2010.

[7] H. A. Atwater and A. Polman, "Plasmonics for improved photovoltaic devices," *Nat. Mater.*, vol. 9, pp. 205–213, 2010.

[8] M. G. Deceglie, V. E. Ferry, A. P. Alivisatos, and H. A. Atwater, "Design of nanostructured solar cells using coupled optical and electrical modeling," *Nano Lett.*, vol. 12, pp. 2894–900, 2012.

[9] V. E. Ferry, A. Polman, and H. A. Atwater, "Modeling light trapping in nanostructured solar cells," *ACS Nano*, vol. 5, pp. 10055–10064, 2011.

[10] R. A. Pala, J. White, E. Barnard, J. Liu, and M. L. Brongersma, "Design of plasmonic thin-film solar cells with broadband absorption enhancements," *Adv. Mater.*, vol. 21, pp. 3504–3509, 2009.

[11] P. Spinelli, M. Hebbink, R. de Waele, L. Black, F. Lenzmann, and A. Polman, "Optical impedance matching using coupled plasmonic nanoparticle arrays," *Nano Lett.*, vol. 11, pp. 1760–1765, Apr. 13, 2011.

[12] J. Grandidier, D. M. Callahan, J. N. Munday, and H. A. Atwater, "Light absorption enhancement in thin-film solar cells using whispering gallery modes in dielectric nanospheres," *Adv. Mater.*, vol. 23, pp. 1272–1276, Mar. 11, 2011.

[13] J. R. Nagel and M. A. Scarpulla, "Enhanced absorption in optically thin solar cells by scattering from embedded dielectric nanoparticles," *Opt. Express*, vol. 18, pp. A139–A146, 2010.

[14] J. Bhattacharya, N. Chakravarty, S. Pattnaik, W. Dennis Slafer, R. Biswas, and V. L. Dalal, "A photonic-plasmonic structure for enhancing light absorption in thin film solar cells," *Appl. Phys. Lett.*, vol. 99, art. no. 131114, 2011.

[15] P. Spinelli, M. A. Verschuuren, and A. Polman, "Broadband omnidirectional antireflection coating based on subwavelength surface Mie resonators," *Nat. Commun.*, vol. 3, art. no. 692, 2012.

[16] J. Zhu, C.-M. Hsu, Z. Yu, S. Fan, and Y. Cui, "Nanodome solar cells with efficient light management and self-cleaning," *Nano Lett.*, vol. 10, pp. 1979–1984, 2010.

[17] V. E. Ferry, M. A. Verschuuren, M. C. V. Lare, R. E. I. Schropp, H. A. Atwater, and A. Polman, "Optimized spatial correlations for broadband light trapping nanopatterns in high efficiency ultrathin film a-Si:H solar cells," *Nano Lett.*, vol. 11, pp. 4239–4245, 2011.

[18] S. B. Mallick, M. Agrawal, and P. Peumans, "Optimal light trapping in ultra-thin photonic crystal crystalline silicon solar cells," *Opt. Express*, vol. 18, pp. 5691–5706, 2010.

[19] J. G. Mutitu, S. Shi, C. Chen, T. Creazzo, A. Barnett, C. Honsberg, and D. W. Prather, "Thin film solar cell design based on photonic crystal and diffractive grating structures," *Opt. Express*, vol. 16, pp. 15238–15248, 2008.

[20] C. Battaglia, C.-M. Hsu, K. Söderström, J. Escarré, F.-J. Haug, M. Charrière, M. Boccard, M. Despeisse, D. T. L. Alexander, M. Cantoni, Y. Cui, and C. Ballif, "Light trapping in solar cells: Can periodic beat random?" *ACS Nano.*, vol. 6, pp. 2790–2797, 2012.

[21] Y. Yao, J. Yao, V. K. Narasimhan, Z. Ruan, C. Xie, S. Fan, and Y. Cui, "Broadband light management using low-Q whispering gallery modes in spherical nanoshells," *Nat. Commun.*, vol. 3, art. no. 664, 2012.

[22] C.-M. Hsu, C. Battaglia, C. Pahud, Z. Ruan, F.-J. Haug, S. Fan, C. Ballif, and Y. Cui, "High-efficiency amorphous silicon solar cell on a periodic nanocone back reflector," *Adv. Energy Mater.*, vol. 2, pp. 628–633, 2012.

[23] M. J. Naughton, K. Kempa, Z. F. Ren, Y. Gao, J. Rybczynski, N. Argenti, W. Gao, Y. Wang, Y. Peng, J. R. Naughton, G. McMahon, T. Paudel, Y. C. Lan, M. J. Burns, A. Shepard, M. Clary, C. Ballif, F. J. Haug, T. Söderström, O. Cubero, and C. Eminian, "Efficient nanocoax-based solar cells," *Phys. Status Solid.—Rapid Res. Lett.*, vol. 4, pp. 181–183, 2010.

[24] J. Kim, A. J. Hong, J.-W. Nah, B. Shin, F. M. Ross, and D. K. Sadana, "Three-Dimensional a-Si:H solar cells on glass nanocone arrays patterned by self-assembled Sn nanospheres," *ACS Nano.*, vol. 6, pp. 265–271, 2011.

[25] X. Li, N. P. Hylton, V. Giannini, K.-H. Lee, N. J. Ekins-Daukes, and S. A. Maier, "Bridging electromagnetic and carrier transport calculations for three-dimensional modelling of plasmonic solar cells," *Opt. Express*, vol. 19, pp. A888–A896, 2011.

[26] H. B. T. Li, R. H. Franken, J. K. Rath, and R. E. I. Schropp, "Structural defects caused by a rough substrate and their influence on the performance of hydrogenated nano-crystalline silicon n–i–p solar cells," *Solar Energy Mater. Solar Cells*, vol. 93, pp. 338–349, 2009.

[27] H. Sakai, T. Yoshida, T. Hama, and Y. Ichikawa, "Effects of surface morphology of transparent electrode on the open-circuit voltage in a-Si:H solar cells," *Jap. J. Appl. Phys.*, vol. 29, pp. 630–635, 1990.

[28] Y. Nasuno, M. Kondo, and A. Matsuda, "Effects of substrate surface morphology on microcrystalline silicon solar cells," *Jap. J. Appl. Phys.*, vol. 40, pp. L303–L305, 2001.

[29] M. D. Kelzenberg, M. C. Putnam, D. B. Turner-Evans, N. S. Lewis, and H. A. Atwater, "Predicted efficiency of Si wire array solar cells," in *Proc. 34th IEEE Photovoltaic Spec. Conf.*, 2009, pp. 001948–001953.

[30] J. Grandidier, R. A. Weitekamp, M. G. Deceglie, D. M. Callahan, C. Battaglia, C. R. Bukowsky, C. Ballif, R. H. Grubbs, and H. A. Atwater, "Solar cell efficiency enhancement via light trapping in printable resonant dielectric nanosphere arrays," *Phys. Status Solidi (A)*, 2012, doi: 10.1002/pssa.201228690.

[31] "FDTD Solutions," (Dec. 1, 2012). [Online]. Available: http://www.lumerical.com

[32] E. Palik and G. Ghosh, *Handbook of Optical Constants of Solids*. New York, NY, USA: Academic, vol. 3, 1997.

[33] A. D. Rakic, A. B. Djurišic, J. M. Elazar, and M. L. Majewski, "Optical Properties of metallic films for vertical-cavity optoelectronic devices," *Appl. Opt.*, vol. 37, pp. 5271–5283, 1998.

[34] "TCAD Sentaurus," [Online]. Available: http://www.synopsys.com

[35] R. E. I. Schropp and M. Zeman, *Amorphous and Microcrystalline Silicon Solar Cells: Modeling, Materials and Device Technology*. Norwell, MA, USA: Kluwer, 1998.

[36] S. Guha, J. Yang, S. J. Jones, Y. Chen, and D. L. Williamson, "Effect of microvoids on initial and light-degraded efficiencies of hydrogenated amorphous silicon alloy solar cells," *Appl. Phys. Lett.*, vol. 61, pp. 1444–1446, 1992.

[37] "AMPS," [Online]. Available: http://www.ampsmodeling.org

[38] "PC1D," [Online]. Available: http://www.pv.unsw.edu.au/info-about/our-school/products-services/pc1 d

[39] "AFORS-HET," [Online]. Available: http://www.helmholtz-berlin.de/forschung/enma/si-pv/projekte/asicsi/afors-het/index_en.html

[40] "SCAPS," [Online]. Available: users.elis.ugent.be/ELISgroups/solar/projects/scaps.html

[41] "ASA," [Online]. Available:http://www.ewi.tudelft.nl/en/the-faculty/departments/electrical-sustainable-energy/photovoltaic-materials-and-devices/asa-software/

Authors' photographs and biographies not available at the time of publication.